COMMUNICATION

BKCS BULLETIN OF THE KOREAN CHEMICAL SOCIETY

Multiple-length scale investigation of Pt/C degradation by identical-location transmission electron microscopy

Jimin Kwag[1,2] (iD) | **Sungin Kim**[1,2] (iD) | **Sungsu Kang**[1,2] (iD) | **Jungwon Park**[1,2,3,4] (iD)

[1]Center for Nanoparticle Research, Institute for Basic Science (IBS), Seoul, Republic of Korea

[2]School of Chemical and Biological Engineering and Institute of Chemical Processes, Seoul National University, Seoul, Republic of Korea

[3]Institute of Engineering Research, College of Engineering, Seoul National University, Seoul, Republic of Korea

[4]Advanced Institutes of Convergence Technology, Seoul National University, Gyeonggi-do, Republic of Korea

Correspondence
Jungwon Park, School of Chemical and Biological Engineering and Institute of Chemical Processes, Seoul National University, Seoul 08826, Republic of Korea.
Email: jungwonpark@snu.ac.kr

Funding information
National Research Foundation of Korea, Grant/Award Number: NRF-2017R1A5A1015365; Institute for Basic Science, Grant/Award Number: IBS-R006-D1; Hyundai Motor Company

Abstract
Pt-based electrocatalysts on the cathode side of proton exchange membrane fuel cells (PEMFCs) generally undergo severe degradation, which contributes to the short life span of PEMFCs. Thus, it is crucial to understand the structural degradation of Pt-based electrocatalysts. Here, various degradation mechanisms of individual Pt nanoparticles supported on Vulcan carbon during load-cycle accelerated stress tests were investigated and quantified by identical-location transmission electron microscopy (IL-TEM). The atomic-scale IL-STEM imaging revealed the formation of Pt single atoms on the carbon support, which resulted from the dissolution of nanoparticles, and the following pathway change in the oxygen reduction reaction (ORR) was analyzed by rotating ring-disk electrode tests. Our study provides new insight for understanding the relationship between the decline in the ORR activity and the formation of Pt atomic species resulting from the electrochemical degradation of Pt/C.

KEYWORDS
degradation mechanism, dissolution, electrocatalyst, fuel cell, IL-TEM

Pt-based nanoparticles are promising candidates for the cathode catalysts of proton exchange membrane fuel cells (PEMFCs) because of their high activity for the oxygen reduction reaction (ORR).[1–8] However, the corrosive environment and high positive potential at the cathode side of PEMFCs tend to deteriorate the activity of the cathode catalyst, which accounts for the short life span of PEMFCs.[9] As the activity of the catalyst is directly determined by the catalyst structure,[6,10–13] understanding the structural degradation of Pt-based catalysts is a prerequisite for designing efficient catalysts with enhanced stability.

The degradation mechanism of Pt/C has been studied by applying an accelerated stress test (AST) to a half-cell[14–16] or membrane electrode assembly.[9,15,17] The AST can simulate certain stressful conditions of real-life operations to induce the degradation of catalysts in a short time.[18] Pt dissolution, one of the primary degradation mechanisms, has been elucidated by analyzing the amount of Pt species in the electrolyte using inductively coupled plasma mass spectrometry.[15,19–21] Carbon corrosion, which is closely associated with the degradation of active Pt catalysts, has been detected by measuring the

concentration of CO_2 using a nondispersive infrared gas analyzer or mass spectrometer.[9,15,22,23] Based on the ensemble information obtained by XRD measurements, structural changes in the Pt catalyst subjected to AST can be used to explain the overall reduction in its catalytic activity and electrochemically active surface area (ECSA).[24,25] In addition, the structural change of nanoparticles in terms of size, morphology, and crystal structure can be understood at the single-particle level by acquiring numerous high-resolution transmission electron microscopy (TEM) images of the catalysts subjected to the AST. Based on the size distribution obtained from the TEM images, the key mechanism for the enlarged Pt nanoparticles observed after the AST, whether due to Ostwald ripening or agglomeration, can be determined.[26] TEM further revealed structural changes in the carbon support, such as the collapse of carbon particle organization or amorphization.[27,28] However, these studies only show ensemble-averaged differences before and after the AST, and it is difficult to identify the exact mechanism that determines the fate of active individual Pt catalyst particles.

Identical-location TEM (IL-TEM) can directly visualize morphological changes in catalyst particles by observing the same locations before and after AST.[29–33] By investigating their structural changes at the single-particle level, IL-TEM enables the explicit specification of the pathways responsible for activity degradation. More importantly, it provides direct evidence of events that cannot be observed using conventional TEM, such as particle detachment.[29,31–33] The results also suggest the coexistence of coalescence and Ostwald ripening, which were considered as two independent mechanisms for the enlargement of particles after AST.[31] Notably, few studies have employed IL-TEM to quantitatively investigate the frequency of different degradation phenomena and their effects on overall activity loss and reduced ECSA. In addition, most studies using IL-TEM have mainly focused on morphological changes in catalysts.[29,31–34] However, various aspects beyond the simple morphological degradation of the active materials remained unclear. For example, Pt atomic species formed by the dissolution of nanoparticles potentially undergo diverse subsequent pathways, such as re-deposition and diffusion to the electrolyte.[1] Thus, a mechanistic understanding of the degradation process of catalysts requires a quantitative comparison of many individual Pt particles before and after AST on a multiple-length scale, starting from a level that discerns morphological changes to an atomic-scale resolution to understand the dynamic behavior of Pt atomic species.

In the present study, IL-TEM was used to investigate the degradation processes of individual Pt nanoparticles supported on Vulcan carbon before and after load-cycle AST, allowing the quantification of various degradation processes, including dissolution, ripening, migration, and coalescence. Atomic-scale imaging using identical-location scanning transmission electron microscopy (IL-STEM), combined with rotating ring-disk electrode (RRDE) tests, revealed that the dissolution of Pt nanoparticles results in the formation of Pt single atoms on the carbon support, which leads to the suppression and enhancement of the four- and two-electron pathways in the ORR, respectively.

The Pt/C catalyst, where 10 wt% of Pt nanoparticles were loaded on Vulcan carbon, was selected as a model system for investigating the degradation processes of the catalysts during the load-cycle AST. The load-cycle AST, a total of 20 000 cycles of square-wave potential cycling between 0.6 and 0.95 V_{RHE}, is typically used to induce the degradation of Pt nanoparticles other than the carbon support.[18] The degradation of Pt nanoparticles supported on Vulcan carbon was studied experimentally using the rotating disk electrode (RDE) technique. To examine the extent of catalyst degradation in terms of catalytic activity or ECSA, basic electrochemical measurements, including cyclic voltammetry (CV) and linear scanning voltammetry (LSV), were conducted before and after the AST (Figure 1a). Structural changes that occur in the catalyst during the AST were identified by IL-TEM, in which the same catalyst particles at identical locations on the catalyst were observed before and after the AST using

TEM/STEM, and the results obtained are compared (Figure 1b). The experimental details are described in the Supporting Information S1.

In both CV curves acquired from the RDE tests before and after the AST, typical characteristics of Pt/C, including hydrogen underpotential deposition (H_{upd}) region (0.05–0.3 V_{RHE}), double layer region (0.3–0.7 V_{RHE}), and Pt–O formation (>0.7 V_{RHE} in the anodic scan), are observed (Figure 1c).[31] The ECSA was determined by calculating the H_{upd} area of the CV curve (details provided in the Supporting Information S1). After conducting the load-cycle AST, the ECSA decreased from 85.822 to 43.842 m^2_{Pt}/g_{Pt}, corresponding to a loss of approximately 48.903%. In the ORR polarization curves of the catalyst before and after the AST, the half-wave potential ($E_{1/2}$) decreased by 48 mV from 0.784 to 0.736 V, as shown in Figure 1e. The reduction in both the ECSA and $E_{1/2}$ values clearly indicates the degradation of Pt/C during the AST.

The structural changes in the same catalyst particles were observed using IL-TEM at various magnifications. The TEM images were acquired at several locations on the Pt/C catalyst before and after the AST, as shown in Figure 2a,b, respectively. The overall shape of the carbon support barely changed (Figure 2a,b), which is in agreement with previous reports.[27,31] Because the massive carbon oxidation reaction mainly occurs at potentials higher than 1.0–1.1 V_{NHE},[27,31] carbon corrosion is not the main process responsible for the degradation of the catalyst as a load-cycle AST was applied in our experiment. Instead, the load-cycle AST induced various structural changes in the Pt nanoparticles, as shown in Figure 2c–h. Based on the results, some nanoparticles did not undergo size change or migration (Figure 2c), some particles grew in size (Figure 2d), some disappeared after the AST (Figure 2e), and new nanoparticles also appeared (Figure 2f). The migration and coalescence of the nanoparticles were also observed, as shown in Figure 2g,h, respectively. These phenomena are consistent with the previously reported mechanisms for Pt/C degradation.[1,31]

In addition to confirming that these processes occur during Pt/C degradation, IL-TEM also allows the quantification of the contribution of each degradation process. The frequency of each degradation process was quantitatively determined by identifying the structural changes in several individual nanoparticles using IL-TEM. The degradation behavior of 266 nanoparticles was analyzed and categorized into six groups: "unchanged," "disappeared," "size change," "migration," "coalescence," and "appeared." Details of the categorization criteria are presented in the Supporting Information S1. Approximately 68% of the nanoparticles remained unchanged at the given spatial resolution, as shown in Figure 2i. Among the nanoparticles that undergo substantial changes, the frequencies of nanoparticles in the "disappeared," "size change," "migration," "coalescence," and "appeared" groups are 12%, 11%, 5%, 4%, and 1%, respectively. The size distributions before and after the AST were determined by measuring the size of
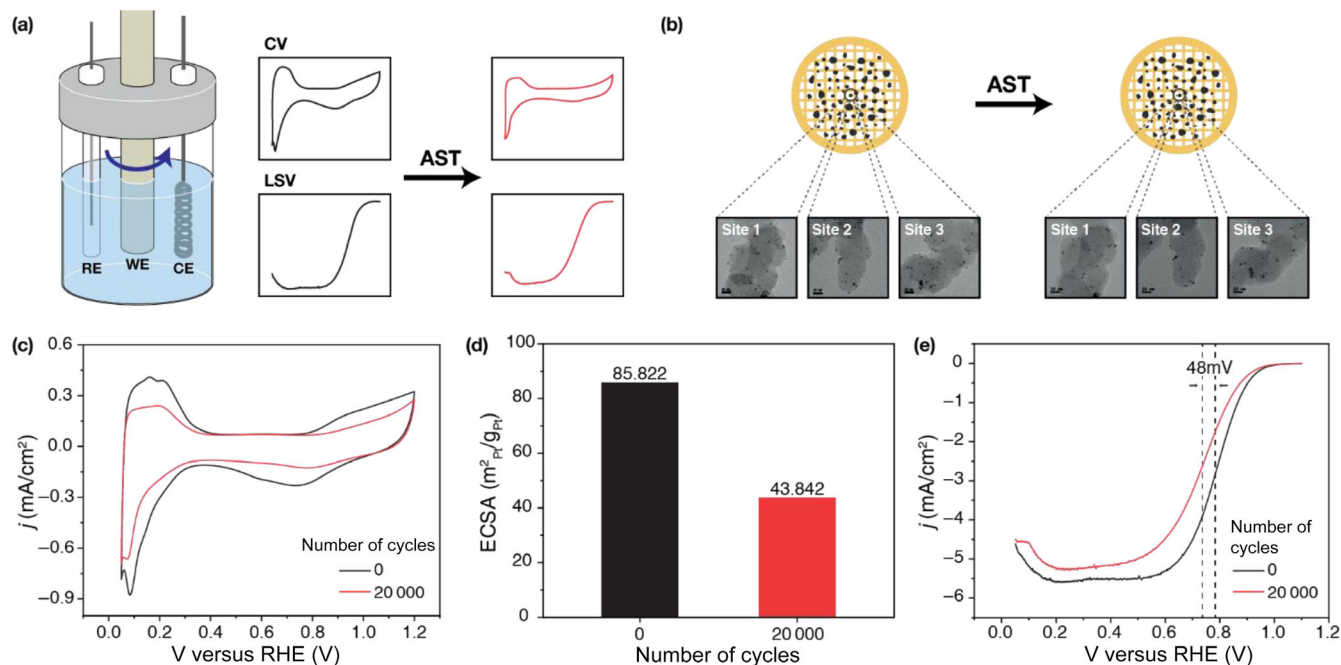
FIGURE 1 (a, b) Scheme on the electrochemical experiments based on rotating disk electrode (RDE) technique and identical-location scanning transmission electron microscopy (IL-TEM) approach, respectively. (c) Comparison of the cyclic voltammograms, (d) electrochemically active surface area (ECSA), (e) polarization curves before and after 20 000 cycles of load-cycle accelerated stress test (AST).

the particles in the images. The average particle size slightly increases from 2.14 to 2.22 nm (Figure 2j,k). The slight change in the size distribution is supported by the fact that a large portion of nanoparticles remained unchanged after applying the load-cycle AST. This is probably due to the relatively small loading of Pt nanoparticles (10 wt%) on the carbon support used in the current study. At large inter-particle distances, the coalescence between particles is likely to be suppressed. Even though the size change or disap-pearance of the nanoparticles clearly contributes to a decline in the ECSA, a discrepancy still exists between the small change in size distribution and the magnitude of the decrease in ECSA after the load-cycle AST. This indicates that the surface of the nanoparticles exists in an electro-chemically deactivated state even though their morphol-ogies remain unchanged after the AST.[35]

The statistics for different types of degradation pro-cesses obtained from the IL-TEM results revealed that the disappearance and size change of the particles were the major degradation mechanisms, as shown in Figure 2i. The disappearance of the nanoparticles can be explained by either particle detachment from the support or dissolu-tion of the Pt nanoparticles. It is difficult to distinguish between these two processes based on the IL-TEM analy-sis. Nonetheless, the dissolution process is supposedly a more major source of particle disappearance than the other process. This is because particle detachment is known to occur when the interaction between the nano-particles and carbon support is weakened by carbon corro-sion.[29,32] The potential applied during the load-cycle AST is insufficient to cause severe carbon corrosion.[27] In addition,

detached particles usually appear on the carbon film of the transmission electron microscopy (TEM) grid when severe particle detachment occurs[31]; however, detached particles were not observed in our IL-TEM results.

The disappearance and size change of the particles, which were the apparent major degradation mechanisms during the AST, are closely related to the dissolution of Pt and diverse subsequent pathways. The dissolution of Pt nanoparticles occurs under repetitive oxidation and reduction of Pt during voltage cycling.[21,36] Pt ions from dissolved nanoparticles can diffuse through the electro-lyte or along the support.[28] Some of them might diffuse into the bulk electrolyte or re-deposit on other nanoparti-cles.[37] These processes decrease the size of the dissolved nanoparticles and promote the growth of the re-deposited nanoparticles, which lead to a change in the size distribu-tion and contribute to a decrease in the ECSA.[38] This phe-nomenon prompts further study on the dynamic behavior of Pt atomic species to elucidate their influence on the overall activity of the catalyst.

Cs-corrected STEM in combination with an identical location technique was used to monitor the pathway of the Pt atomic species resulted from the dissolution of the Pt nanoparticles. The IL-STEM images taken before and after the AST are shown in Figure 3a,b, respectively. The images are color coded to improve the visibility. The Pt element is distinguishable by its darker contrast than that of the carbon support. Regions showing notable changes are marked with dotted boxes, as shown in Figure 3a,b, whereas the magnified images are presented in Figure 3c. The size of the Pt particles decreased due to dissolution,
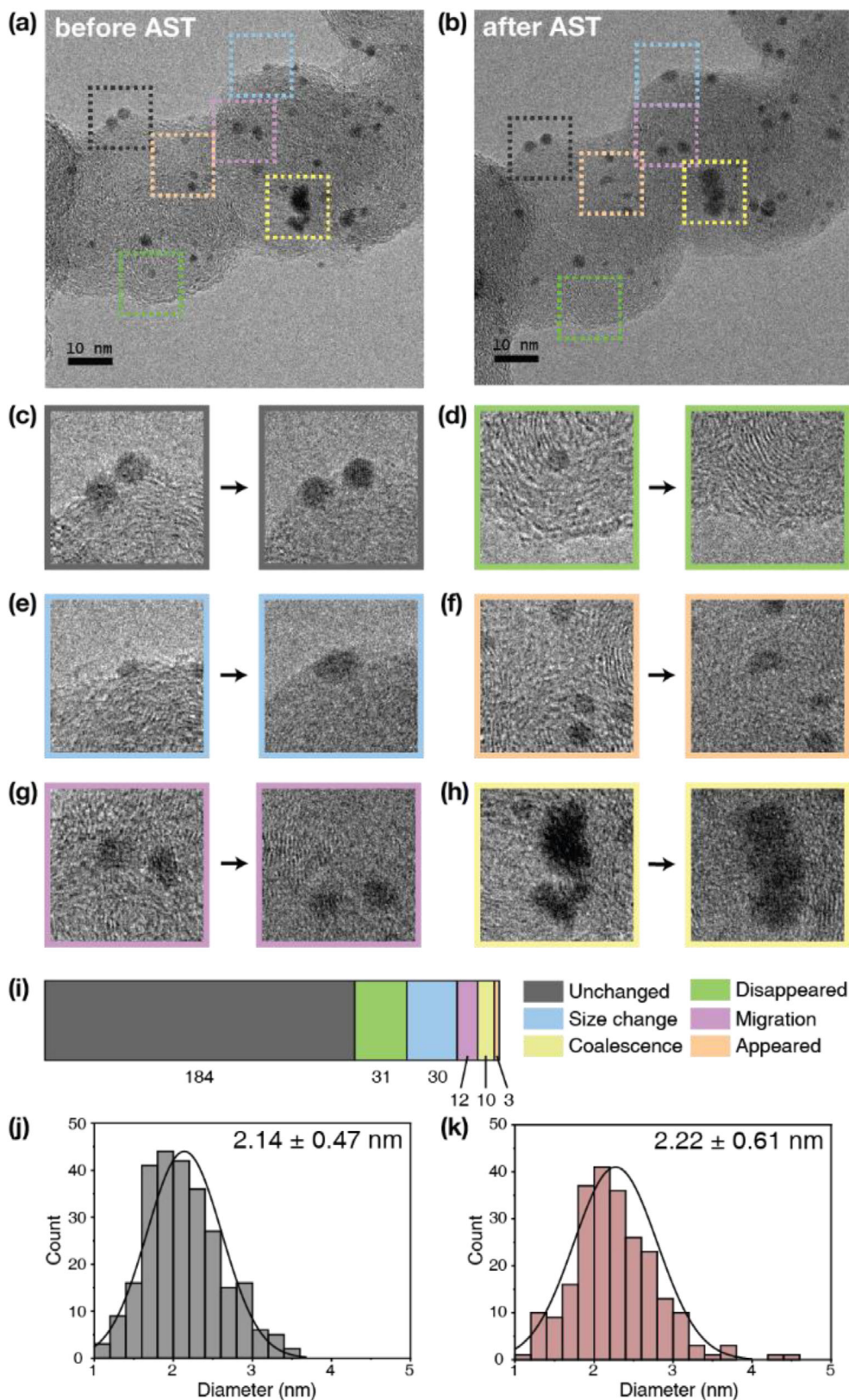
FIGURE 2 Representative identical-location transmission electron microscopy (IL-TEM) image of Pt/C (a) before and (b) after accelerated stress test (AST). Regions are marked with boxes in in gray, green, blue, orange, purple, and yellow, which are examples for each category, "unchanged," "disappeared," "size change," "migration," "coalescence," and "appeared," respectively. Magnified images of the marked regions are presented in (c)–(h). (i) Frequencies of each categorized process. (j, k) Histograms of particle diameter before and after accelerated stress test (AST), respectively.
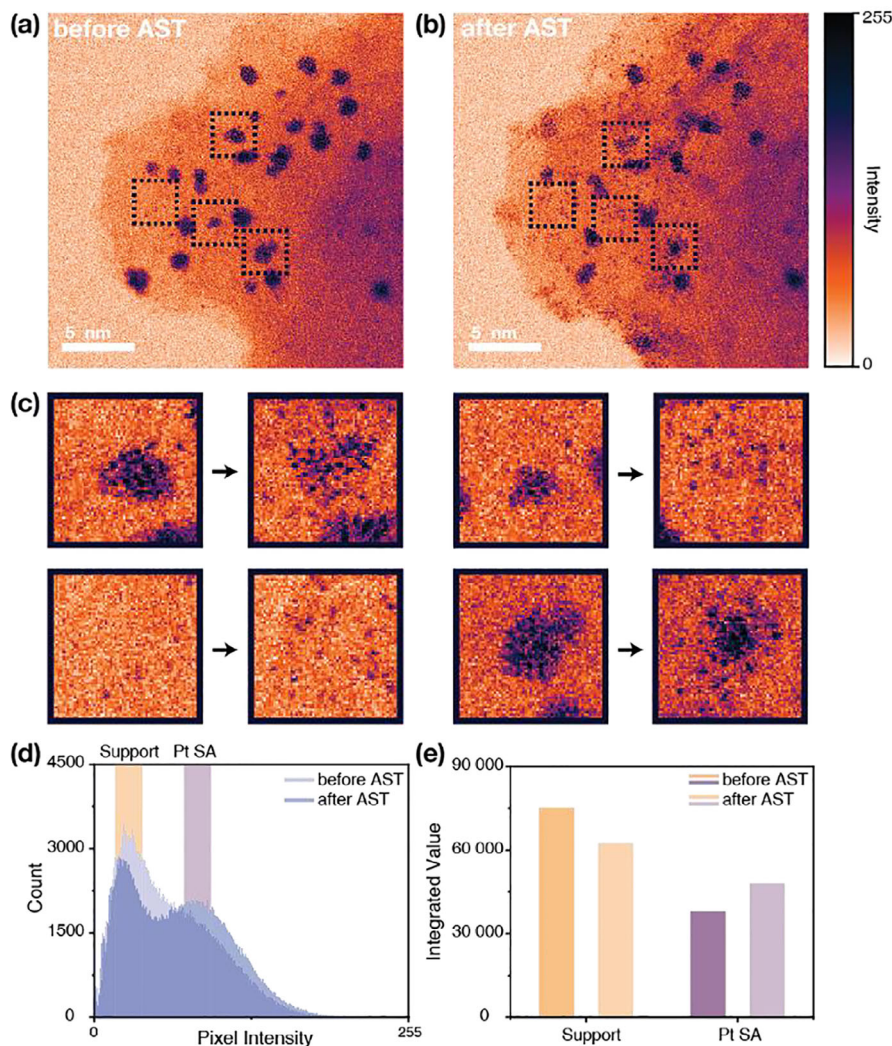
FIGURE 3 Representative identical-location scanning transmission electron microscopy (IL-STEM) image of Pt/C (a) before and (b) after AST. Images were color coded for visibility. Regions with notable changes are marked with dotted boxes. (c) Magnified images of the marked regions in (a) and (b). (d) Histograms showing the pixel intensity of the images before and after AST. (e) Comparison of the integrated values for the peaks of the histogram.

and a notable amount of Pt single atoms appeared near those particles, as shown in Figure 3c. In addition, some Pt single atoms appeared on the carbon support in the regions where nanoparticles were absent initially (left images in the bottom row in Figure 3c). An attempt was made to quantify the increased number of Pt single atoms on the support. Visible Pt nanoparticles were excluded from the images (Supporting Information S1), and a histogram of pixel intensity was acquired from each image (Figure 3d,e). The two main peaks in the pixel intensity distribution (Figure 3d) are distinguished as follows: lower intensity (orange) and higher intensity (purple), which correspond to the carbon support and Pt single atoms, respectively. The area of the histogram for each peak was integrated and compared. After the AST, the integrated value for the carbon support peak decreased, whereas the value for the Pt single-atom peak increased, as shown in Figure 3e. These results demonstrate that after the AST,

the Pt atomic species from the dissolved nanoparticles were deposited on the carbon support and appeared as Pt single atoms.

Pt nanoparticles are known to catalyze the four-electron reduction pathway desired for the conversion of O_2 to H_2O as Pt ensemble sites enable side-on adsorption of O_2, which leads to cleavage of the O—O bond.[39] In contrast, Pt single atoms tend to catalyze the two-electron reduction pathway, which converts O_2 to H_2O_2, because of the absence of an ensemble site.[39] The IL-STEM results (Figure 3) show the dissolution of the nanoparticles and the formation of the Pt single atoms on the carbon support, implying the possibility of the suppression of four-electron pathway while enhancing two-electron pathway. The RRDE test, which enabled us to quantify the H_2O_2 formation rate, was conducted to investigate the changes in the ORR pathway as the catalyst underwent degradation. In the RRDE test, O_2 was reduced at the disk to either
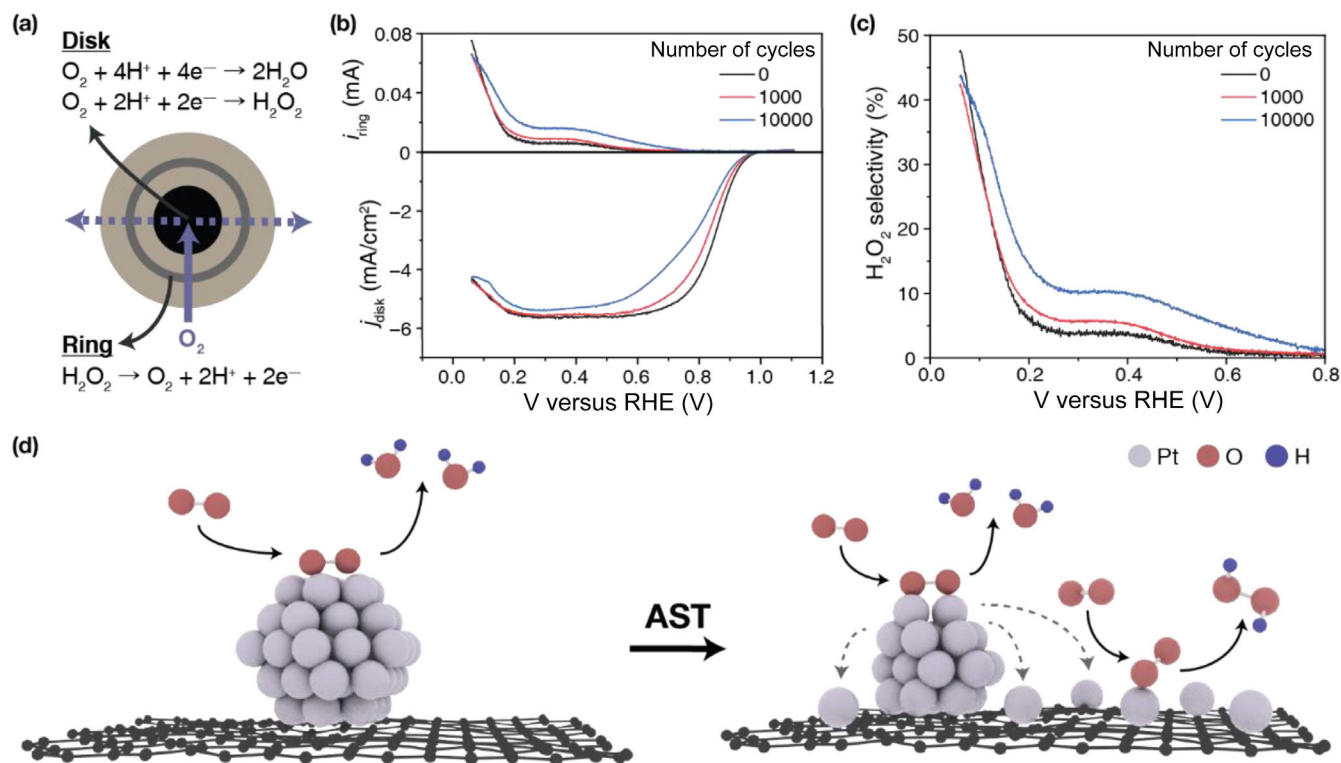
FIGURE 4 (a) Scheme illustrating the reactions on rotating ring-disk electrode (RRDE). At the disk, O_2 is reduced to either H_2O or H_2O_2. At the ring, H_2O_2 is oxidized back to O_2. (b) Ring current and disk current recorded from the RRDE test after 0, 1000, and 10 000 cycles of accelerated stress test (AST). (c) H_2O_2 selectivity after 0, 1000, and 10 000 cycles of AST. (d) Scheme illustrating the formation of Pt single atoms on the carbon support during AST and their effect on ORR pathway. Pt atomic species resulted from particle dissolution deposits on the carbon support and catalyzes two-electron pathway, producing H_2O_2.

H_2O_2 or H_2O, whereas H_2O_2 was oxidized back to O_2 at the ring (Figure 4a). The ring and disk currents were collected after 0, 1000, and 10 000 cycles of AST and are presented in Figure 4b. The selectivity for H_2O_2 and electron transfer number (n) were calculated from the collected currents (details provided in the Supporting Information S1). During the AST, the selectivity for H_2O_2 increased (Figure 4c), whereas the electron transfer number decreased (Supporting Information S1), indicating that the four-electron pathway catalyzed by the Pt nanoparticles is suppressed, whereas the two-electron pathway catalyzed by the Pt single atoms is enhanced, as shown in Figure 4d. The RRDE test confirmed that the formation of the Pt single atoms, which provides a route to alter the electrochemical pathway of the ORR, observed in the IL-STEM images generally occurs during the application of load-cycle AST.

CONCLUSION

In summary, we investigated the degradation process of Pt nanoparticles supported on Vulcan carbon during the load-cycle AST at multiple-length scales and its influence on the overall activity loss. The quantitative analysis of the degradation processes, enabled by the particle-by-particle approach using IL-TEM, revealed that the structural changes in the nanoparticles were mainly caused by Pt dissolution and various subsequent processes. The IL-STEM results suggest that the deposition of the Pt atomic species as single atoms on the carbon support is an important pathway taken by the dissolved Pt ions formed from the dissolution of the catalytic nanoparticles. Based on the RRDE test results, the formation of the Pt single atoms on the support leads to a change in the ORR pathway. Our study highlights the importance of high-resolution imaging to understand the behavior of atomic species during catalyst degradation.

ORCID

Jimin Kwag https://orcid.org/0000-0002-2014-1586
Sungin Kim https://orcid.org/0000-0001-9107-0781
Sungsu Kang https://orcid.org/0000-0001-8220-0345
Jungwon Park https://orcid.org/0000-0003-2927-4331

REFERENCES

[1] J. C. Meier, C. Galeano, I. Katsounaros, J. Witte, H. J. Bongard, A. A. Topalov, C. Baldizzone, S. Mezzavilla, F. Schüth, K. J. Mayrhofer, *Beilstein J. Nanotechnol.* **2014**, *5*, 44.

[2] R. L. Borup, A. Kusoglu, K. C. Neyerlin, R. Mukundan, R. K. Ahluwalia, D. A. Cullen, K. L. More, A. Z. Weber, D. J. Myers, *Curr. Opin. Electrochem.* **2020**, *21*, 192.

[3] H. Y. Kim, J. Y. Kim, S. H. Joo, *Bull. Korean Chem. Soc.* **2021**, *42*, 724.

[4] L. Huang, S. Zaman, X. Tian, Z. Wang, W. Fang, B. Y. Xia, *Acc. Chem. Res.* **2021**, *54*, 311.

[5] N. Jung, D. Y. Chung, J. Ryu, S. J. Yoo, Y.-E. Sung, *Nano Today* **2014**, *9*, 433.

[6] Y.-J. Wang, W. Long, L. Wang, R. Yuan, A. Ignaszak, B. Fang, D. P. Wilkinson, *Energy Environ. Sci.* **2018**, *11*, 258.

[7] D. Y. Chung, J. M. Yoo, Y. E. Sung, *Adv. Mater.* **2018**, *30*, 1704123.

[8] S. G. Ji, H. C. Kwon, T.-H. Kim, U. Sim, C. H. Choi, *ACS Catal.* **2022**, *12*, 7317.

[9] S. Kreitmeier, A. Wokaun, F. N. Büchi, *J. Electrochem. Soc.* **2012**, *159*, F787.

[10] J. Qian, M. Shen, S. Zhou, C.-T. Lee, M. Zhao, Z. Lyu, Z. D. Hood, M. Vara, K. D. Gilroy, K. Wang, *Mater. Today* **2018**, *21*, 834.

[11] G. S. Harzer, A. Orfanidi, H. El-Sayed, P. Madkikar, H. A. Gasteiger, *J. Electrochem. Soc.* **2018**, *165*, F770.

[12] S. W. Han, D. H. Kim, I. H. Kim, Y. D. Kim, *Bull. Korean Chem. Soc.* **2016**, *37*, 674.

[13] H. L. Xin, E. A. Pach, R. E. Diaz, E. A. Stach, M. Salmeron, H. Zheng, *ACS Nano* **2012**, *6*, 4241.

[14] H. A. Gasteiger, S. S. Kocha, B. Sompalli, F. T. Wagner, *Appl. Catal. B: Environ.* **2005**, *56*, 9.

[15] E. Pizzutilo, S. Geiger, J.-P. Grote, A. Mingers, K. J. J. Mayrhofer, M. Arenz, S. Cherevko, *J. Electrochem. Soc.* **2016**, *163*, F1510.

[16] Z.-M. Zhou, Z.-G. Shao, X.-P. Qin, X.-G. Chen, Z.-D. Wei, B.-L. Yi, *Int. J. Hydrog.* **2010**, *35*, 1719.

[17] P. Ferreira, Y. Shao-Horn, D. Morgan, R. Makharia, S. Kocha, H. Gasteiger, *J. Electrochem. Soc.* **2005**, *152*, A2256.

[18] A. Ohma, K. Shinohara, A. Iiyama, T. Yoshida, A. Daimaru, *ECS Trans.* **2011**, *41*, 775.

[19] D. Johnson, D. Napp, S. Bruckenstein, *Electrochim. Acta* **1970**, *15*, 1493.

[20] S. Cherevko, G. P. Keeley, S. Geiger, A. R. Zeradjanin, N. Hodnik, N. Kulyk, K. J. Mayrhofer, *ChemElectroChem* **2015**, *2*, 1471.

[21] A. Pavlišič, P. Jovanovič, V. S. Šelih, M. Šala, N. Hodnik, M. Gaberšček, *J. Electrochem. Soc.* **2018**, *165*, F3161.

[22] Y. Li, Z. Zheng, X. Chen, Y. Liu, M. Liu, J. Li, D. Xiong, J. Xu, *Int. J. Hydrog.* **2020**, *45*, 23519.

[23] S. Maass, F. Finsterwalder, G. Frank, R. Hartmann, C. Merten, *J. Power Sources* **2008**, *176*, 444.

[24] R. Sharma, S. M. Andersen, *Appl. Catal. B: Environ.* **2018**, *239*, 636.

[25] Z.-B. Wang, P.-J. Zuo, Y.-Y. Chu, Y.-Y. Shao, G.-P. Yin, *Int. J. Hydrog.* **2009**, *34*, 4387.

[26] Y. Zhang, S. Chen, Y. Wang, W. Ding, R. Wu, L. Li, X. Qi, Z. Wei, *J. Power Sources* **2015**, *273*, 62.

[27] L. Castanheira, W. O. Silva, F. H. Lima, A. Crisci, L. Dubau, F. d. R. Maillard, *ACS Catal.* **2015**, *5*, 2184.

[28] J. C. Meier, C. Galeano, I. Katsounaros, A. A. Topalov, A. Kostka, F. Schüth, K. J. Mayrhofer, *ACS Catal.* **2012**, *2*, 832.

[29] K. J. Mayrhofer, J. C. Meier, S. J. Ashton, G. K. Wiberg, F. Kraus, M. Hanzlik, M. Arenz, *Electrochem. Commun.* **2008**, *10*, 1144.

[30] H. Yun, J. Kim, W. Choi, M. H. Han, J. H. Park, H.-s. Oh, K. Kwak, Y. J. Hwang, *Electrochim. Acta* **2021**, *371*, 137795.

[31] A. Zana, J. Speder, M. Roefzaad, L. Altmann, M. Bäumer, M. Arenz, *J. Electrochem. Soc.* **2013**, *160*, F608.

[32] K. J. Mayrhofer, S. J. Ashton, J. C. Meier, G. K. Wiberg, M. Hanzlik, M. Arenz, *J. Power Sources* **2008**, *185*, 734.

[33] K. Schlögl, M. Hanzlik, M. Arenz, *J. Electrochem. Soc.* **2012**, *159*, B677.

[34] F. J. Perez-Alonso, C. F. Elkjær, S. S. Shim, B. L. Abrams, I. E. Stephens, I. Chorkendorff, *J. Power Sources* **2011**, *196*, 6085.

[35] K. Higashi, G. Samjeské, S. Takao, T. Kaneko, O. Sekizawa, T. Uruga, Y. Iwasawa, *J. Phys. Chem. C* **2017**, *121*, 22164.

[36] A. A. Topalov, S. Cherevko, A. R. Zeradjanin, J. C. Meier, I. Katsounaros, K. J. Mayrhofer, *Chem. Sci.* **2014**, *5*, 631.

[37] R. Borup, J. Meyers, B. Pivovar, Y. S. Kim, R. Mukundan, N. Garland, D. Myers, M. Wilson, F. Garzon, D. Wood, *Chem. Rev.* **2007**, *107*, 3904.

[38] Z. Zheng, F. Yang, C. Lin, F. Zhu, S. Shen, G. Wei, J. Zhang, *ACS Appl. Mater. Interfaces* **2020**, *12*, 35088.

[39] S. Yang, J. Kim, Y. J. Tak, A. Soon, H. Lee, *Am. Ethnol.* **2016**, *55*, 2058.

SUPPORTING INFORMATION

Additional supporting information can be found online in the Supporting Information section at the end of this article.